High-Performance Thermoelectric Bulk Colusite by Process Controlled Structural Disordering

Cedric Bourges, Yohan Bouyrie, Andrew R. Supka, Rabih Al Rahal Al Orabi, Pierric Lemoine, Oleg I. Lebedev, Michihiro Ohta, Koichiro Suekuni, Vivian Nassif, Vincent Hardy, et al.

High-performance Thermoelectric Bulk Colusite by Process Controlled Structural Disordering

Cédric Bourgès, Yohan Bouyrie,[†] Andrew R. Supka,[†] Rabih Al Rahal Al Orabi,[#] Pierric Lemoine, Oleg I. Lebedev, Michihiro Ohta, Koichiro Suekuni, Vivian Nassif, Vincent Hardy, Ramzy Daou, Yuzuru Miyazaki, Marco Fornari* and Emmanuel Guilmeau**

C. Bourgès, Dr. O.I. Lebedev, Dr. V Hardy, Dr. R. Daou, Dr. E. Guilmeau

Laboratoire CRISMAT, UMR 6508, CNRS, ENSICAEN, 6 Boulevard du Maréchal Juin, 14050 Caen Cedex 04, France

E-mail: emmanuel.guilmeau@ensicaen.fr

Dr. Y. Bouyrie, Dr. M. Ohta

Research Institute for Energy Conservation, National Institute of Advanced Industrial Science and Technology (AIST), Tsukuba, Ibaraki 305-8568, Japan

Dr. P. Lemoine

Institut des Sciences Chimiques de Rennes (ISCR) - UMR CNRS 6226, Rennes, France

Dr. K. Suekuni

Department of Applied Science for Electronics and Materials, Interdisciplinary Graduate School of Engineering Sciences, Kyushu University, Kasuga, Fukuoka 816-8580, Japan

Dr. V. Nassif

Univ. Grenoble Alpes, F-38000 Grenoble, France & CNRS, Inst. NEEL, F-38042 Grenoble, France

Dr. Y. Miyazaki

Department of Applied Physics, Graduate School of Engineering, Tohoku University, Sendai 980-8579, Japan

A. R. Supka, Dr. R. Al Rahal Al Orabi,[#] Dr. M. Fornari

Department of Physics and Science of Advanced Materials Program, Central Michigan University, Mt. Pleasant, MI 48859, USA

E-mail: marco.fornari@cmich.edu

E-mail: rabih.orabi@solvay.com

Abstract

High-performance thermoelectric bulk sulfide with the colusite structure is achieved by controlling the densification process and forming short-to-medium range structural defects. A simple and powerful way to adjust carrier concentration combined with enhanced phonon scattering through point defects and disordered regions is described. By combining experiments with band structure and phonons calculations, we elucidate, for the first time, the underlying mechanism at the origin of intrinsically low thermal conductivity in colusite samples as well as the effect of S vacancies and antisite defects on the carrier concentration. Our approach provides a controlled and scalable method to engineer high power factors and remarkable figures of merit near the unity in complex bulk sulfide such as $Cu_{26}V_2Sn_6S_{32}$ colusites.

[#] Present address : Solvay, Design and Development of Functional Materials Department, AXEL'ONE Collaborative Platform - Innovative Materials, 87 Rue des Freres Perret – BP62, 69192 Saint Fons Cedex

1. Introduction

The design and optimization of thermoelectric (TE) materials rely on the intricate balance between thermopower (S), electrical resistivity (ρ) and thermal conductivity (κ); perfecting such a balance is key to improve energy recovery systems and thermoelectric cooling devices.[1] A host of materials has been investigated in the past,[2–4] often neglecting the need to reconcile efficiency with environment and cost constraints both from a composition and/or a processing perspective. For instance, telluride based materials exhibit good performances[5–13] but are of value only for niche applications due to the escalating prize of tellurium and other less costly compositions require synthesis approaches that are scalable to industrial settings.

Copper sulfides can provide an eco-friendly high-performance low cost alternative since often they contain elements that are abundant in naturally occurring minerals. The values of the figure of merit, $ZT = S^2T/\rho\kappa$, observed in $Cu_{2-x}S$, range from 0.5 to 1.7 (at T = 1000 K) making this material very promising.[14–16] However, the electro-migration of copper noted in the Cu-S system weakens the stability and their potential for TE applications.[14,17] In order to mitigate electro-migration, other metallic species besides copper have been added into the composition extending the exploration to complex ternary/quaternary Cu based sulfides. A non-exhaustive list includes p-type tetrahedrite $Cu_{12-x}Tr_xSb_4S_{13}$ ($ZT \sim 0.80$ @ 700 K)[18–31] with Tr = Mn, Fe, Co, Ni, Zn ($x \leq 2$), colusite $Cu_{26}V_2Sn_6S_{32}$ ($ZT \sim 0.60$ @ 700 K),[32,33] germanite-derivative $Cu_{22}Fe_8Ge_4S_{32}$ ($ZT \sim 0.17$ @ 575 K),[34] bornite Cu_5FeS_4 ($ZT \sim 0.55$ @ 550 K),[35–37] stannoidite $Cu_{8.5}Fe_{2.5}Sn_2S_{12}$ ($ZT \sim 0.35$ @ 630 K),[38] Cu_2SnS_3 ($ZT \sim 0.56$ @ 750 K),[39] Cu_2ZnSnS_4 ($ZT \sim 0.35$ @ 700 K)[40,41], $CuCr_{2-x}Sb_xS_4$ ($ZT \sim 0.45$ @ 650 K)[42] or n-type $Cu_4Sn_7S_{16}$ ($ZT \sim 0.21$ @ 700 K),[43] $CuFeS_2$ ($ZT \sim 0.17$ @ 630 K),[44,45] $Cu_2CoTi_3S_8$ ($ZT \sim 0.18$ @ 650 K)[46] and $CuFe_2S_3$ ($ZT \sim 0.14$ @ 700 K).[47]

Regardless the light atomic masses, most of these materials exhibit low thermal conductivity possibly determined by local structural distortions, rattling phenomena, or strong bond anharmonicity. In $Cu_{12}Sb_4S_{13}$ tetrahedrite, for instance, a low-energy phonon excitation is manifested by the out-of-plane motion of Cu atoms located in specific crystal site ($12e$) which induces scattering effects. It has been pointed out that this anisotropic atomic motion is also favored by the Sb lone pair localized above and below the trigonal plane.[19,21,48,49] The low thermal conductivity in other Cu based sulfides was vaguely attributed to the complexity of the crystal structure.[32,33,35,39,43]

Colusite, $Cu_{26}V_2Sn_6S_{32}$, represents a prototypical complex sulfide (*i.e.* large unit cell with 66 atoms and light mass elements) with low lattice thermal conductivity, κ_L.[32] It has been recently studied but the origin of the low thermal conductivity is not understood and the full potential of $Cu_{26}V_2Sn_6S_{32}$ as an advanced thermoelectric material has not been fully explored. In additional, there are significant discrepancies in the measured properties. Values for the lattice thermal conductivity (κ_L) for the pristine phase are ranging from 0.50–0.55 W m^{-1} K^{-1},[28,32,50] to around 0.90–1.35 W m^{-1} K^{-1},[33,51] at 350K. These two different behaviors seem intimately related to the intrinsic crystallographic structure and the presence of defects. Indeed, by carefully comparing the electrical properties, it can be established that the samples with higher κ_L values are more metallic with S as low as 30 µV K^{-1} and ρ around 0.6 mΩ cm at 300K. In comparison, samples with low κ_L values exhibit S of 100–130 µV K^{-1} and ρ in the range 3.5–6.0 mΩ cm. This observation indicates interesting sensitivity of the heat and electronic transport to structural features induced by different processing methods (powder synthesis and densification techniques).

We present here a complete study of the bulk properties of colusite including, for the first time, the characterization of the band structure and the vibrational dispersions from first principles calculations. We pinpoint the special role played by Cu in low frequency optic

modes and linked such an effect with electronic properties. More importantly, we prove that the TE transport properties of colusite are dramatically influenced by the densification temperature and method, and suggest strategies to control the formation of specific defects. Transport properties and TE efficiency are rationalized within these novel findings in order to provide guidance for the design of TE materials based on tailoring the role of defects.

2. Results and discussion

For clarity, this section is arranged by grouping various data by observations and conclusions they generate. First, the band structure and vibrational dispersions from first principles calculations of the pristine $Cu_{26}V_2Sn_6S_{32}$ are presented. The specific structural features are then explored by means of X-ray/neutron diffraction and transmission electron microscopy. This is followed by the characterization of the electrical and thermal properties whose data are discussed in relation with band structure/vibrational dispersions calculations and structural analysis.

2.1. Band Structure and phonon dispersions

Pristine colusite, $Cu_{26}V_2Sn_6S_{32}$, has a complex cubic structure (space group $P\bar{4}3n$, N° 218) [52] formed by a sulfur corner-sharing tetrahedral network (*8e*, and *24i*) centered around Cu (*6d*, *8e*, and *12f*) and Sn (*6c*). The V (*2a*) atoms occupy a body centered cubic sublattice and are surrounded by S in *8e* (**Figure 1**).

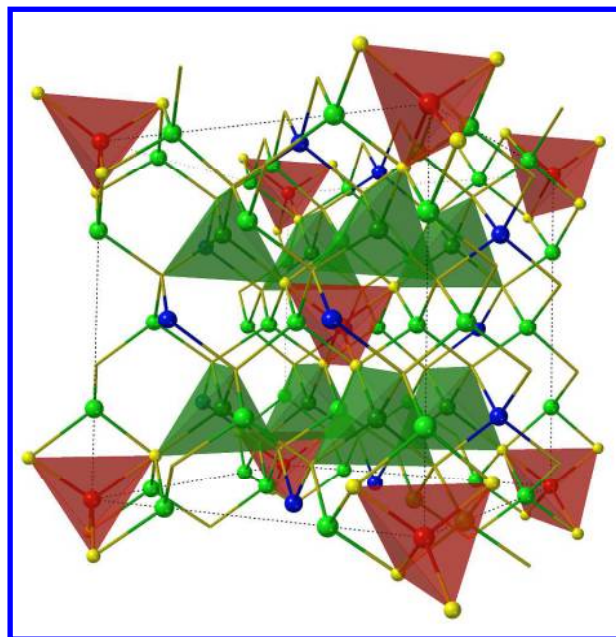**Figure 1.** Unit cell of $Cu_{26}V_2Sn_6S_{32}$ (space group $P\bar{4}3n$, N° 218). We show the S in $8e$ (yellow) bridging V (red) with Cu $8e$ (dark green). Cu in $6d$ and $12f$ are in light green, Sn in blue, and S in $24f$ are not shown. First principles computed structural parameters are in good agreement with experiments: a = 10.797 Å, Cu ($12f$, $x = 0.748$), Cu ($8e$, $x = 0.753$), Cu ($6d$), Sn ($6c$), V($2a$), S ($24i$ x = 0.867, $y = 0.369$, $z = 0.119$), and S ($8e$, $x = 0.620$).

Depending on the oxidation states of V and Sn (we tentatively assumed Cu^{1+} and S^{2-}), we expect from 4 to 14 holes per unit cell. Indeed, the Fermi level (E_F) crosses the valence manifold 0.26 eV below the onset of an energy gap of about 1 eV (**Figure 2**). The Fermi level lies in the valence manifold indicating a *p*-type metallic behavior, which is in agreement with the experimental transport properties (Figure 8). Integration of the density of states (DOS) from E_F to the onset of the energy gap indicates a holes concentration of about 38×10^{20} cm^{-3} at room temperature which is consistent with V^{5+} and Sn^{4+}.

The top of the valence band exhibits a multi-valley character with large effective masses

especially at Γ, X, and M high-symmetry points in the cubic Brillouin zone. As expected, electronic states in the proximity of E_F originate from the hybridization between the sulfur p-orbitals (mainly from S in $24i$) and substantial contributions from the Cu $3d$-orbitals. The conduction band exhibits an isolated flat manifold below 1.5 eV (energies are measured with respect to E_F) mostly associated with V d-orbitals with contribution from the S atom in $8e$. The electronic structure seems to indicate that the V atoms form strong ionic bonds with the surrounding S ($8e$, tetrahedral coordination) and, in turn, soften the S($8e$)-Cu($8e$) bonds as seen in the S-Cu longer distance. This can be justified by the substantial difference in electronegativity between Cu and V.
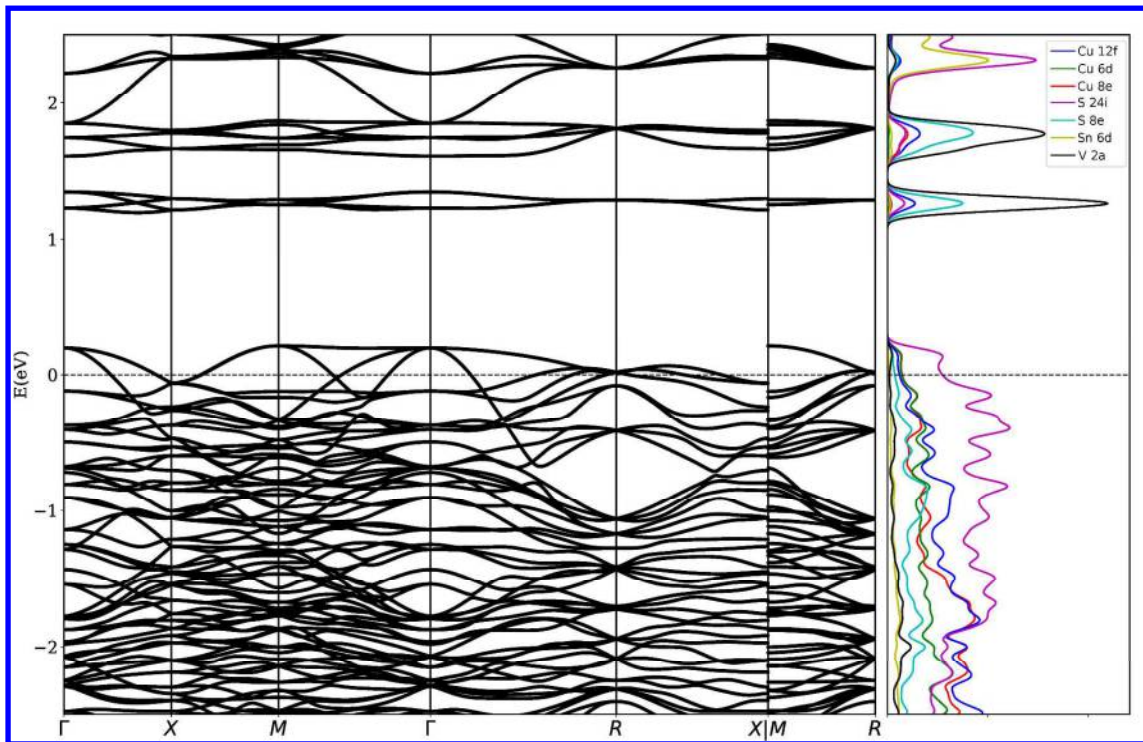

Figure 2. Electronic band structure and atom projected electronic density of states of $Cu_{26}V_2Sn_6S_{32}$. Hubbard U corrections were computed self-consistently within the ACBN0 approach (see text): U(Cu in $12f$) = 7.82, U(Cu in $8e$) = 7.69, U(Cu in $6d$) = 7.78, U(V) = 0.02, U(Sn) = 0.00, U(S in $24i$) = 1.11 and U(S in $8e$) = 1.13.

As mentioned in the introduction, the origin of the low thermal conductivity of $Cu_{26}V_2Sn_6S_{32}$ is not understood. We explored the origin of the low thermal conductivity by using density functional theory (DFT) calculations of phonon dispersions and atom-resolved vibrational DOS (VDOS, **Figure 3**). Although calculations within the harmonic approximation do not provide direct information on the thermal conductivity, the phonon dispersions show compressed acoustic branches which lead to low heat carrier velocity and low thermal conductivity.[53,54] Also, the presence of low frequencies optic modes (40 and 60 cm^{-1}) that can interact with the acoustic vibrations is known to introduce scattering channels that affect the thermal conductivity.[55,56] This conjecture agrees with the observations in BiOCuS and skutterudites materials that have very low thermal conductivities.[55,57–59] To better characterize the low frequency modes, we computed the VDOS projected on the atoms, as shown in Figure 3. Surprisingly the largest contribution at low frequency is associated to Cu in 8*e* crystallographic site. Due the light mass of Cu, we must assume very soft bonds near Cu in 8*e* and assign a major role to its chemical environment on the thermal transport properties as observed in the electronic band structure. This is in agreement with computed total energy response to bond compression for the three Cu sites that point to softer bonds for the Cu in *8e* (**Figure S1**). However, more investigations, such as temperature dependent neutron diffraction powder analysis, are needed in order to clarify this point. Quantities derived from our first principles phonon dispersion such as sound velocity and specific heat are also in excellent agreement with the experimental measurements. We computed an average sound velocity of 3150 m/s (υ_T = 2350 m s^{-1}, $\upsilon_{T'}$ = 2613 m s^{-1} and υ_L = 4485 m s^{-1}) and a Debye temperature of 367 K. Experimentally, from specific heat capacity measurements, the Debye temperature was calculated in the range of 350-375 K (**Figure S2**, Supplementary Information). This corresponds to an average sound velocity of 3017-3230 m s^{-1}. The longitudinal sound velocity was also confirmed by direct measurements (υ_L = 4260 m

s^{-1}).

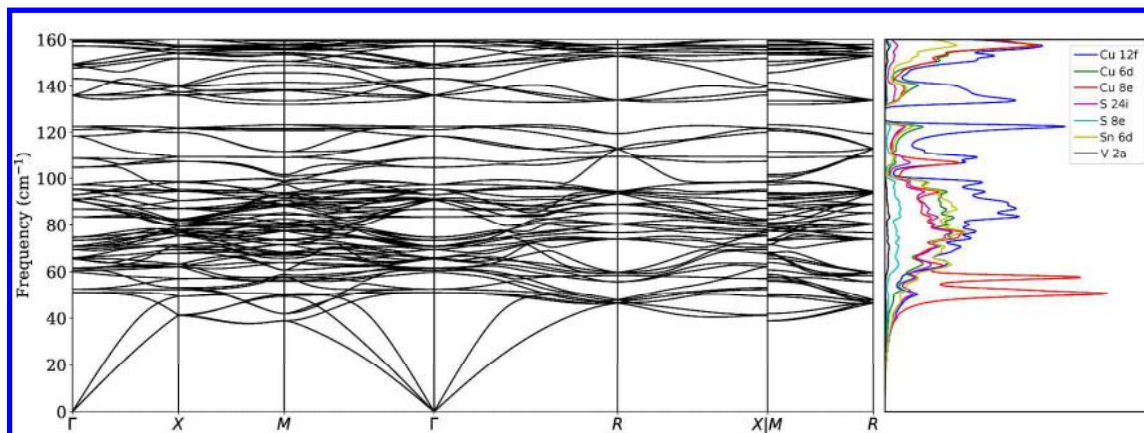**Figure 3.** Phonon dispersions and atom-projected vibrational density of states of Cu$_{26}$V$_2$Sn$_6$S$_{32}$. Optic modes at frequency as low as 40 cm^{-1} contribute to scattering phenomena that lower the lattice thermal conductivity. Notice the prominent role of Cu in 8e at low frequency.

2.2. Synthesis and structural characterization

Our goal is to understand and optimize the TE properties of colusite using cost effective and scalable methods. We chose to perform reproducible powder synthesis by mechanical-alloying. This technique produces a fine and homogeneous black powder for which the X-ray diffraction data refinements are consistent with the cubic $P\bar{4}3n$ space group and cell parameters (a = 10.79(1) Å) expected for colusite.[51] The obtained powders were then densified using two different consolidation techniques, *i.e.* spark plasma sintering (SPS) at 873 K (sample L (Low T))[51] and hot pressing (HP) at 1023 K (sample H (High T)).[50] The phase purity and crystallinity of the two sintered colusite samples have been confirmed by combined Rietveld refinement of X-ray powder diffraction (XRPD) and neutron powder diffraction (NPD) patterns both recorded at room temperature (**Figure 4** and **S3**, respectively).

Structural parameters determined from these refinements are gathered in **Table S1** and **Table S2** (bonds distances). The refinements confirm the reported structure but point to some differences on the peak positions and intensities between the two patterns. Indeed, combined Rietveld refinements of the XRPD and NPD patterns lead to slightly larger refined cell parameter for sample H (a = 10.8289(2) Å) compared to sample L (a = 10.7701(2) Å). These results suggest the possible existence of structural defects in sample H and a slight deviation of the expected chemical composition. This conjecture is supported by energy dispersive X-ray spectroscopy (EDX) spot analysis performed on twenty grains of each sample. The approximate average compositions (**Table S3**) are as following: $Cu_{27.3}V_{1.9}Sn_{6.0}S_{31.4}$ for the two samples sintered at 1023 K (sample H) and $Cu_{25.0}V_{1.9}Sn_{6.0}S_{32.6}$ for the two samples sintered at 873 K (sample L). From these semi-quantitative analyses, we can distinguish a clear tendency towards a copper-rich and sulfur-poor composition for the sample H. Also, larger composition standard deviations are observed in sample H as compared to sample L. The copper-rich chemical composition combined with larger composition standard deviations and significant larger cell parameter refined for the sample H suggests a degree of mix random occupation of the Cu, Sn and V sites with possible S vacancies and atom insertion as interstitials.[50] Most of these defects influence the carrier concentration and should have effects on the transport properties. It is also implicit that minor traces of Sn/V rich phases may exist, even if not detected from XRD/NPD and scanning/transmission electron microscopy analyses.
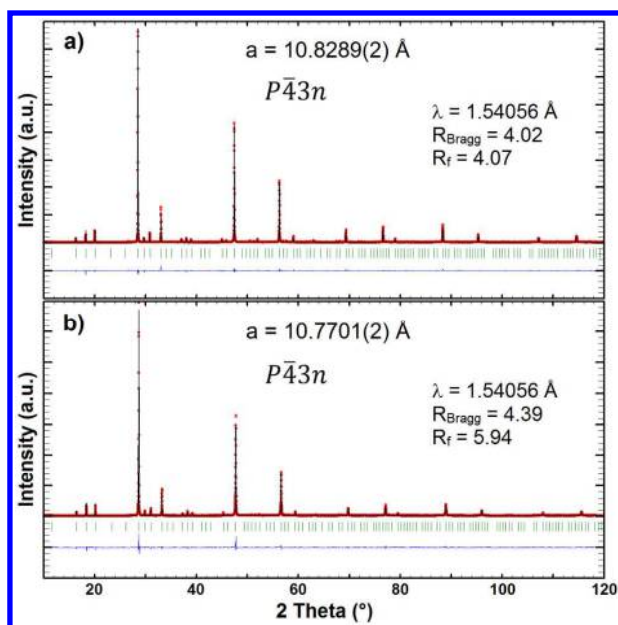
Figure 4. Rietveld refinements of the XRPD patterns recorded at room temperature of the samples H (a) and L (b), sintered respectively at 1023 K and 873 K.

In order to determine the crystallographic defects in this sample, several structural models were tested to refine the XRPD and NPD data. While attempts to insert metallic atoms in the interstitial $6b$ (0, 0, ½) and/or $24i$ (~0, ~¼, ~¼) sites did not improve the initial model, slightly better refinements were obtained considering a partial substitution of V atoms ($2a$ site) and/or Sn atoms ($6c$ site) by Cu atoms. Nevertheless, such metal site random occupancy cannot be determined unambiguously from XRPD and NPD data only but requires complementary local probe investigations such as TEM or resonant contrast diffraction (RCD). To confirm the crystal structure and investigate further the possible formation of structural defects at the atomic level, TEM studies, including electron diffraction (ED) and high angle annular dark field scanning TEM (HAADF-STEM), were undertaken. Several crystallites analyses performed on both samples highlighted that their structure are generally well crystallized in agreement with XRPD and NPD data. The main zones of the $Cu_{26}V_2Sn_6S_{32}$ ED patterns (**Figure 5**) and its corresponding HAADF-STEM images show a

perfectly crystallized structure, which can be indexed based on the cubic $P\bar{4}3n$ ($a \sim 10.8$ Å) structure, obtained from XRPD and NPD data.
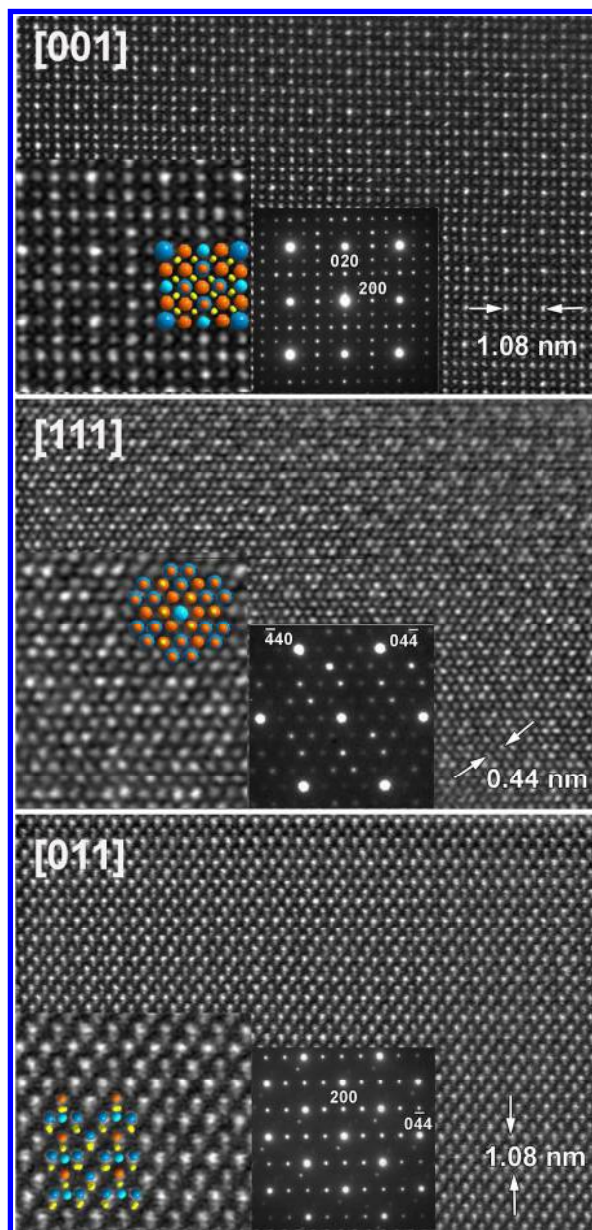

Figure 5. Typical HAADF-STEM images and corresponding ED patterns of both samples L and H sintered respectively at 873 K or 1023 K for main zone axis [001], [111] and [011]. The three figures are representative of both samples L and H. Enlargement images with the overlaid structural models are given as insert. (Sn-blue, V-light blue, Cu-orange, S-yellow)

No defect regions or superstructures have been found for the sample sintered at 873 K
(sample L). On the contrary, TEM analysis of the sample sintered at 1023 K (sample H)
revealed different structural defects/features. The [001] HAADF-STEM image (**Figure 6a**)
clearly shows the presence of 1D line of point defects. One observes three main sorts of
atomic columns intensities. Bearing in mind that contrast in HAADF-STEM image is directly
proportional to the thickness and atomic number ($\sim Z^2$), each column can be attributed to a
decaying level of brightness, from pure Sn ($Z = 50$) to a mixed Sn/V ($23 < Z < 50$) and pure
Cu ($Z = 29$) (**Figures 5 and 6c**). In this respect, it is obvious that the 1D line defects result
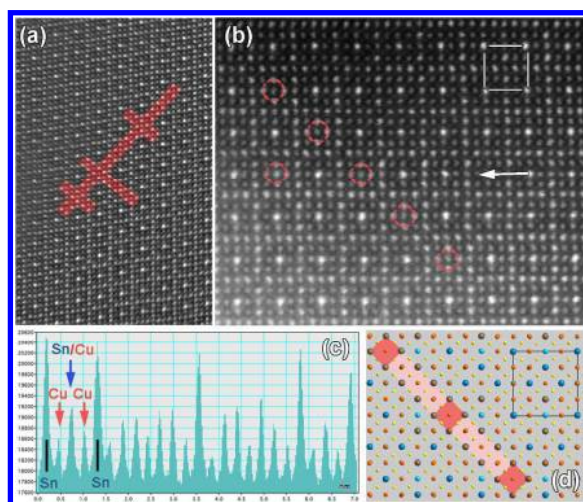from the Sn substitutions with V and/or Cu (**Figure 6b**).

Figure 6. (a) [001] HAADF-STEM image of sample H sintered at 1023 K. Red color
indicates 1D line defects distributed within the perfect crystal of $Cu_{26}V_2Sn_6S_{32}$. (b)
Enlargement part of line defect. Red circle depicted Sn-site defects columns. (c) Intensity line
scan profile along the atomic layer indicated by white arrow in (b). There is a clear violation
of Sn columns periodicity (higher peaks in the plot profile) corresponding to Sn-site defects.
Note that the peak intensity of Sn-site defects columns is similar to those of pure Cu column
suggesting the substitution of Sn by Cu atoms. (d) Corresponding structural model of the 1D
Sn-vacancy line defect.

A careful inspection of the images reveals the presence of Sn columns with significantly reduced contrast compared to the regular bright contrast of pure Sn columns (note the intensity profile in **Figure 6c)**. The observed contrast intensity is qualitatively similar to pure Cu contrast intensity, hence, suggesting the substitution of Sn with Cu. Due to the lack of spurious Sn-rich phases, however, it is reasonable to assume concurrent random occupation of V and/or Cu sites with Sn. It should be also noted that such Sn substitutions by Cu and V were found distributed randomly over the crystal although. Considering the sizes of the tetrahedra (V tetrahedron smaller than Cu tetrahedron smaller than Sn tetrahedron) and the chemical composition, the Sn-Cu antisites are also expected to be kinetically more probable. Also, total energy calculations for the formation energies of antisite defects (**Table 1**) indicate that the Cu-Sn antisites involving Cu $6d$ and Cu $8e$ are favored. The Cu $6d$ and $8e$ sites form channels around the Sn sites (**Figure S4**, Supplementary Information) leading to a tendency to form 1D defects lines. We speculate that ordering along the line (…-Sn-Sn-Cu-Sn-Sn-…) is forced by electrostatic repulsion.

In addition, in some other areas, we observed a clear tendency to form larger 3D disordered regions, as it is shown in **Figure 7.** These ordered and disordered areas are coherently intergrown with equivalent structural frameworks and unit cell parameters. These results agree with the observations of different domains of ordered and disordered cations in a colusite natural mineral $Cu_{24.3}V_{2.0}(As_{5.7}Sb_{0.6}Fe_{0.1})S_{32}$, as stressed by Spry et $al.$[52] They assume that the disordered regions might correspond to a derived sulvanite-type structure. Finally, from the different structural investigations (XRPD, NPD and HAADF-STEM) and chemical analyses (EDX), we can conclude that the samples sintered at 873 K are well crystallized and ordered, while increasing the sintering temperature up to 1023 K favors sulfur volatilization and the creation of short-to-medium range structural defects. Conjunction of S volatilization and high temperature during hot-pressing at 1023 K probably favor a balance between

entropy-governed disordered phase and internal energy-governed ordered phase. It verifies the hypothesis proposed by Spry *et al.*, that the disordered domain is the stable form at high temperature. Further experiments will be necessary to establish accurately the crystallization temperature windows and kinetics of formation of such disordered and ordered domains using different densification methods (SPS or HP).

Table 1. Formation energies (in meV) for antisites defects in colusite.

	Sn/V	Sn/Cu 12f	Sn/Cu 6d	Sn/Cu 8e	V/Cu 12f	V/Cu 6d	V/Cu 8e
ΔE (meV)	33	42	19	25	21	40	31
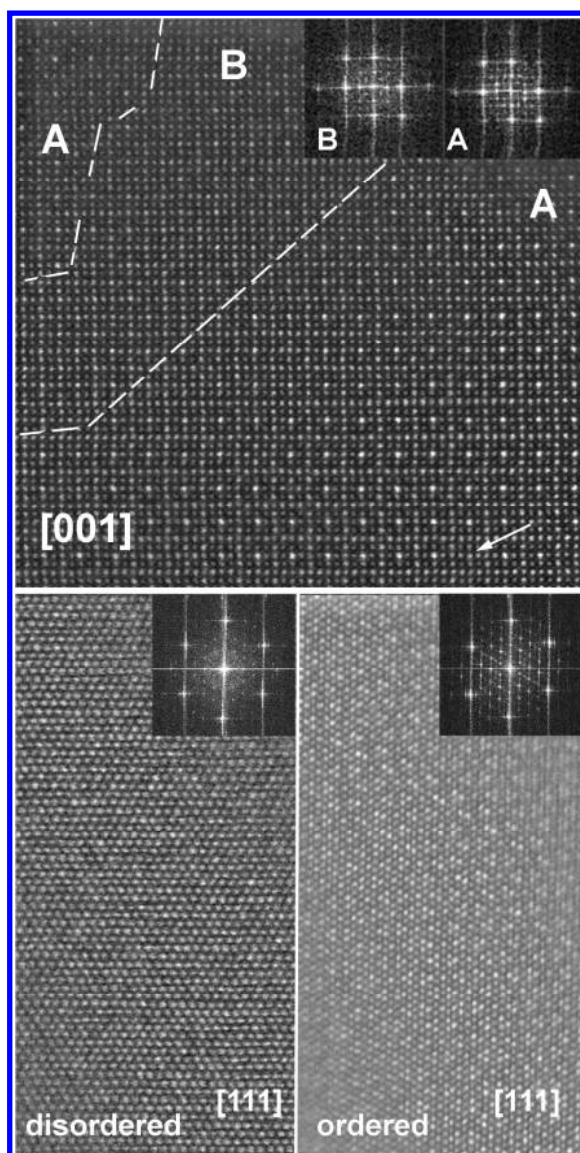
Figure 7. [001] and [111] HAADF-STEM images showing the coexistence of ordered an disordered regions within the same crystallite in the sample H sintered at 1023 K. Corresponding FT patterns are given as inset. Row indicates a point defect.

2.3. Electrical and thermal transport properties

Figure 8a and 8b show, respectively, the electrical resistivity ρ and Seebeck coefficient S of two batches of samples differently sintered over the temperature range 300–675K. All the properties measurements were performed on four ingots, two sintered at 873 K and two sintered at 1023 K (samples L and H, respectively). Both ρ and S increase with temperature and the positive sign of S confirms the p-type carrier of colusite, in agreement with the electronic structure calculations. A small dispersion of the electrical properties is observable for both sets of samples, which is consistent with deviation from ideal stoichiometry of colusite.[28] Overall, samples H exhibit higher ρ and S compared to the other ones sintered at 873 K. The magnitudes of the electrical properties are in good agreement with previous studies, where two distinct electrical behaviors were observed, *i.e.* metallic-like[33,51] and another less conducting behavior.[28,32,50] In our measurements, ρ and S evolve at room temperature from 0.4–1.0 mΩ cm and 30–45 μV K^{-1} in the samples L, to 1.9–2.8 mΩ cm and to 90–101 μV K^{-1} in the samples H. The significant increase of ρ and S values observed in the latter sample is likely governed by the sulfur deficiency (as mentioned above) due to the volatilization of sulfur during hot pressing at high temperature (1023 K for 1h).

The carrier concentration of sample L was extracted from Hall measurements. The value of 32.6×10^{20} cm^{-3} is in good agreement with the computed value of 38×10^{20} cm^{-3}, acknowledging the presence, in a small amount, of S vacancies (with an estimated concentration of about 0.8 vacancies per unit cell). Defects are affecting the transport

properties by modifying the charge carrier density and by introducing scattering phenomena that influence the relaxation time (both for charge carriers and heat carriers). We noted earlier that the samples H sintered at 1023 K are S poor and Cu rich and, additionally, our structural analysis indicates a degree of disorder in the occupation of Sn, V, and Cu sites. S vacancies introduce electrons ($\square_S^{2\bullet} + 2e' + 26\ Cu_{Cu}^X + 6\ Sn_{Sn}^X + 31\ S_S^X + 2\ V_V^X$) whereas V-Sn antisites ($V_{Sn}^{\bullet} + Sn_V' + 26\ Cu_{Cu}^X + 5\ Sn_{Sn}^X + 32\ S_S^X + V_V^X$), Cu-Sn antisites ($Cu_{Sn}^{3'} + Sn_{Cu}^{3\bullet} + 25\ Cu_{Cu}^X + 5\ Sn_{Sn}^X + 32\ S_S^X + 2\ V_V^X$), and V-Cu antisites ($Cu_V^{4'} + V_{Cu}^{4\bullet} + 25\ Cu_{Cu}^X + 6\ Sn_{Sn}^X + 32\ S_S^X + 1\ V_V^X$) do not seem to modify the carrier concentration. Experimentally, Hall effect characterization indicates, for samples H, a lower carrier concentration of 13.5×10^{20} cm^{-3} that may be imputed to partial compensation of the intrinsic hole population due to S vacancies (comparing theoretical data on pristine colusite we estimated that the vacancies density is roughly 1.5 defects per unit cell, the double with respect to samples L). An alternative possibility is that the decrease in the holes concentration is due to the presence of interstitial copper cations ($Cu_i^{\bullet} + e' + 26\ Cu_{Cu}^X + 6\ Sn_{Sn}^X + 32\ S_S^X + 2\ V_V^X$).[50] However, this would require larger defect density that was not evidenced from the structural analysis. From a structural point of view, the smaller unit cell and shorter Cu-S bond distances observed in sample L (Tables S1 and S2) may be also an indication of its larger Cu(II) content. However, the correlation between hole concentration and bond distances in the two samples must be taken with caution due the disordered character of sample H. Finally, the Hall mobilities are about 4.3 cm^2 V^{-1} s^{-1} for samples L and 2.1 cm^2 V^{-1} s^{-1} for samples H in agreement with the additional scattering effects associated with mass and chemical disorder on the metal sites. (see **Figure S5**).

In addition to possibly introduce charge carriers in the crystal, defects modify the electronic structure and may influence indirectly the carrier concentration. By performing calculations, we noted that Sn-Cu antisites do modify indirectly the charge concentration

increasing it from 38×10^{20} cm^{-3} to 46×10^{20} cm^{-3} (T = 300 K). Using this new value for the theoretical carrier concentration, sample H may have an excess of holes that, in order to reconcile theory and experiments, should be compensated by additional S vacancies (with a total concentration of about 2 vacancy/unit cell if we exclude other compensating mechanisms). To estimate the effect of defects on electronic relaxation time, we have fitted theoretical calculations performed in the constant relaxation time approximation to the experimental measurements of the resistivity and estimated the temperature effect on the relaxation time. Results point to a scattering time of sample H 2.5 – 3.0 times larger than the one of sample L. Interestingly enough, the simultaneous increase of carrier concentration due to local rearrangement of the electronic structure and scattering time due to S vacancy formation modifies significantly the electrical properties.

The power factor (*PF*) temperature dependences, presented in **Figure 8e**, shows that both sample batches reach similar values at high temperature with a maximum ranging around 0.70 – 0.75 mW m^{-1} K^{-2} at 675K. These values are in good agreement with previous studies on $Cu_{26}V_2Sn_{6-x}S_{32}$ (with $x = 0.5$)[28] or $Cu_{26}Ta_2Sn_6S_{32}$ colusites,[50] but remain lower than the value of 0.92 mW m^{-1} K^{-2} reported at 700 K for the $Cu_{25}ZnV_2Sn_6S_{32}$ composition.[51]
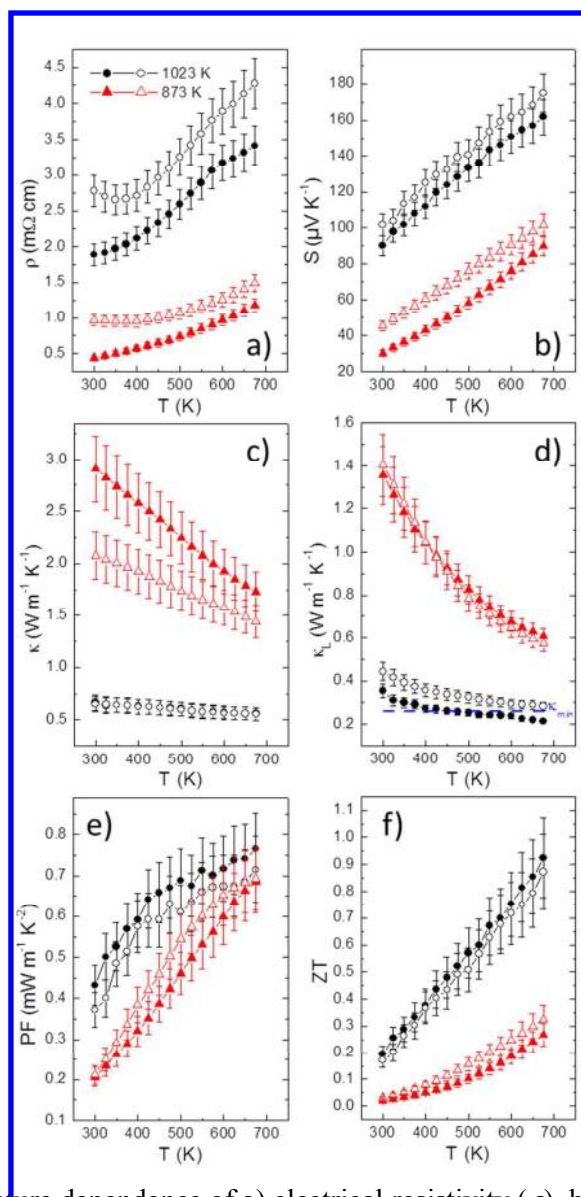
Figure 8. Temperature dependence of a) electrical resistivity (ρ), b) Seebeck coefficient (S) c) thermal conductivity (κ), d) lattice thermal conductivity (κ_L), e) power factor (PF), and f) dimensionless figure of merit ZT of samples L and H, sintered at 873 K and 1023 K, respectively.

The temperature dependences of the total (κ) and the lattice component (κ_L) of the thermal

conductivity are presented in **Figures 8c** and **8d**, respectively. All the samples evidence a decrease of κ from 300 K to 675 K. However, two distinct magnitudes for both κ and κ_L are clearly visible depending on the sintering temperature. As previously reported,[51] mechanical-alloyed powders sintered at 873 K have relatively high κ values of 2.1–2.9 W m^{-1} K^{-1} at 300 K and 1.4–1.7 W m^{-1} K^{-1} at 675 K. This large magnitude is linked to i) the metallic behavior and the large carrier contribution to the thermal conductivity ($\kappa_e \sim$ 0.8–1.5 W m^{-1} K^{-1} at 300 K) and ii) the absence of structural defects (as seen above). Furthermore, it is obvious that increasing sintering temperature up to 1023 K induces a remarkable decrease in κ with ultra-low values of 0.65–0.67 W m^{-1} K^{-1} at 300 K and 0.55–0.56 W m^{-1} K^{-1} at 675 K, as reported earlier.[28,32,48,50] The κ reduction can be attributed to i) the decrease of κ_e ($\sim$ 0.3–0.4 W m^{-1}K^{-1} at 300 K) and ii) the enhanced phonon scattering induced by the existence of structural defects leading to a more disordered character of the samples sintered at 1023 K. κ_L is then reduced on the full temperature range with a significant decrease from 1.3 W m^{-1} K^{-1} for the samples sintered at 873 K to 0.3–0.4 W m^{-1} K^{-1} for the samples sintered at 1023 K, which is close to the computed theoretical minimum lattice thermal conductivity (k_{min} = 0.27 W m^{-1} K^{-1}) using the shortest scattering distance within the model proposed by Cahill *et al.*[60]

Based on our structural analyses, the origin of the low lattice thermal conductivity in samples H is mainly attributed to the scattering effects induced by S vacancies and cationic disorder, that scatters short-wavelength phonons. In addition, the ordered and disordered regions are coherently intergrown, and their interfaces can also contribute to scattering of phonons with medium wavelengths, meanwhile maintaining good carrier transport without excessive scattering.[10,61] This statement is also supported by the decrease of the measured sound velocities from 4260 m s^{-1} in sample L down to 3620 m s^{-1} in sample H. Such a reduction indicates that defects modify the vibrational spectrum in addition to introduce additional

scattering for the heat carriers. Hence, these structural features are unique in terms of enhancing the thermoelectric performances of colusite.

Finally, the temperature dependence of the dimensionless figure of merit, *ZT*, is given in **Figure 8f**. All samples exhibit similar temperature dependence with a maximum *ZT* value of 0.93 at 675K for the sample sintered at 1023 K. To the best of our knowledge, this is the highest value reported for Sn-based bulk colusite. Compared to the samples sintered at 873 K, there is an improvement of around 300% of the figure of merit at 675K. This huge enhancement takes place in the full temperature range.

3. Conclusion

We have performed an in-depth analysis of $Cu_{26}V_2Sn_6S_{32}$ to illustrate the potential of this complex sulfide for thermoelectric applications. Using scalable mechanical alloying synthesis and different densification methods, we demonstrated how point defects can be used to engineer thermoelectric materials. The measurements are rationalized with the aid of total energy and band structure calculations as well as the calculation of harmonic vibrational properties. Our findings include: (1) the thermoelectric properties of colusite can be tailored with appropriate densification strategies, (2) the measured low thermal conductivity is due to the presence of soft Cu vibration at low frequency combined with the scattering effects induced by S vacancies and chemical disorder on the metal ions sublattices, (3) the endotaxial nature of this disordered region does not compromise the power factor, (4) lines of point defects form spontaneously because of the specific energetics of antisite defects.

As a result, the *ZT* value of bulk colusites rises to near unity at 675K, making this material one of the best *p*-type TE materials in this temperature region. This approach can be extended to other ternary/quaternary metal/semiconductors with the aim to synthesize other disordered TE materials with enhanced performances. This work thus addresses the interest of

researchers to broaden the scope of prospective TE materials especially among complex sulfide systems.

4. Experimental Section

Mechanically alloyed powders of $Cu_{26}V_2Sn_6S_{32}$ were prepared by milling 5g of copper (Alfa Aesar, 99.5 %), vanadium (Alfa Aesar, 99.5 %), sulfur (Alfa Aesar, 99.5 %), and tin (Merck, 99.9 %) in stoichiometric proportions in a planetary ball mill (Fritsch Pulverisette 7 Premium line). The milling was performed during 12h at a speed of 600 rotations per minute under argon atmosphere in a 45 mL tungsten carbide jar containing 10 balls of 10 mm diameter. It produces a fine black powder. X-ray powder diffraction data collected on this material are consistent with the $P\bar{4}3n$ space group and cell parameters expected for colusite as reported elsewhere.[51] The obtained powder was then densified using two different consolidation techniques: 1) spark plasma sintering (SPS – FCT HPD 25)) during 45 minutes at 873 K under a uniaxial pressure of 64 MPa with cooling and heating rates of 50 K min^{-1} with a slight over pressure of +50 hPa (Ar) and 2) hot pressing (HP FUT-17000, TOKYO VACUUM) at 1023 K for 1 h under a uniaxial pressure of 70 MPa in Ar gas flow of 300 ml min^{-1} with heating and cooling rates of 10 K min^{-1} and 20 K min^{-1}, respectively. Two ingots were produced for both densification techniques. The geometrical densities of sample L and H are respectively 90.1% and 89.5% of the theoretical values determined from XRPD data.

XRPD measurements were performed using a D8 advance diffractometer with silicium band lynx eyes detector (Cu Kα radiation with Ge (111) monochromator). Data were collected with the addition of 6 scans over the angular range $10 \leq 2\theta/° \leq 120$ with a step size of 0.0105°, and a step time of 1.3 sec. NPD experiments were carried out at the Institut Laue Langevin (ILL), Grenoble, France. Data were collected at 300K using the high-flux neutron

two-axis powder diffractometer D1B (λ = 1.28 Å) equipped with position sensitive detector of 1280 cells covering a total of 128°.

XRPD and NPD patterns were simultaneously refined by Rietveld analysis using the *FullProf* and *WinPlotr* software packages.[62,63] The shape of the diffraction peaks was modelled using a Thompson-Cox-Hastings pseudo-Voigt profile function.[64] Zero-point shift and asymmetry parameters were systematically refined, and the background contribution was manually estimated. Lattice parameter, atomic positions, and isotropic displacement parameters (*i.e.* Debye-Waller factors: B_{iso}) were finally refined and gathered in Table S1. Bond distances are presented in Table S2.

Energy dispersive X-ray spectroscopy (EDAX EDX detector) spot analyses were performed on twenty grains of each sample (Table S3).

Transmission electron microscopy (TEM) analyses including electron diffraction (ED) and high angle annular dark field scanning TEM (HAADF-STEM) studies were performed by using a JEM200F cold FEG image and probe aberration microscope operated at 200 kV, equipped with CENTURIO EDX detector and Quantum GIF. TEM samples were prepared by crushed powder in agate mortar, suspended in n-butanol and then deposited on a Ni holey carbon grid.

The electrical resistivity (ρ) and Seebeck coefficient (*S*) were measured simultaneously from ingots, from 300 K up to 675 K using ULVAC-ZEM3 device under partial helium pressure. An LFA–457 model was used for measuring the thermal diffusivity under argon flow. The thermal conductivity (κ) was determined as the product of the geometrical density, the thermal diffusivity and the theoretical heat capacity using Dulong-Petit approximation. Zero-field heat-capacity measurements were also carried out from 5 K to 300 K in the same device using a relaxation method with a 2τ fitting procedure (**Figure S2**).

The Wiedemann-Franz law was used to calculate the lattice thermal conductivity by

subtracting the electronic contribution to the total thermal conductivity ($\kappa_L = \kappa - \kappa_e$). Here, the Lorenz number L was estimated as function of temperature from the experimental Seebeck coefficients using single parabolic band model[65] ($L(T)$ curves are displayed in **Figure S6**). The estimated measurements uncertainties are 6% for the Seebeck coefficient, 8% for the electrical resistivity, 11% for the thermal conductivity and 16% for the final figure of merit, ZT.[66] Room temperature Hall effect measurements were carried out using Physical Properties Measurement System (PPMS; Quantum Design) under an applied magnetic field up to 9T.

Band structures and phonon dispersions were computed using AFLOWπ,[67,68]. We used ultrasoft PBE pseudopotentials, well converged basis sets corresponding to an energy cut-off of 60 Ry for the wavefunctions and 600 Ry for the charge density. To integrate over the Brillouin zone we used a 4 x 4 x 4 grid. Hubbard U corrections were computed within the (Agapito-Curtarolo-Buongiorno Nardelli (ACBN0) approach,[69,70] providing the values in Figure 2. For the ACBN0 we used norm-conserving pseudopotentials (E_{cut} = 150 Ry). Electronic transport and carrier concentrations have been computed using interpolated tight-binding hamiltonians as in Ref.[71]

Supporting Information

Supporting Information is available from the Wiley Online Library or from the author.

Figure S1. Total energy response to the cationic displacement.

Figure S2. Specific heat capacity as a function of temperature.

Figure S3. Rietveld refinement of the NPD patterns.

Figure S4. Structural channels formed by Cu 6d and 8e around the Sn sites.

Figure S5. Relaxation time fitted to experimental data on the resistivity.

Figure S6: Lorentz number as a function of temperature.

Table S1. Structural parameters determined from combined XRPD/NPD data Rietveld refinements.

Table S2. Interatomic bond distances (Å).

Table S3. Atomic compositions determined by EDS.

Author Information

[†] Y.B. and A.R.S. contributed equally to this work.

References

(1)   Bell, L. E. *Science* **2008**, *321*, 1457.

(2)   Snyder, G. J.; Toberer, E. S. *Nat. Mater.* **2008**, *7* (2), 105.

(3)   Koumoto, K.; Mori, T. *Thermoelectric Nanomaterials, Springer: New York*; 2013.

(4)   Tan, G.; Zhao, L. D.; Kanatzidis, M. G. *Chem. Rev.* **2016**, *116*, 12123.

(5)   Pei, Y.; Shi, X.; LaLonde, A.; Wang, H.; Chen, L.; Snyder, G. J. *Nature* **2011**, *473*, 66.

(6)   Sootsman, J. R.; Chung, D. Y.; Kanatzidis, M. G. *Angew. Chemie - Int. Ed.* **2009**, *48*, 8616.

(7)   Hsu, K. F.; Loo, S.; Guo, F.; Chen, W.; Dyck, J. S.; Uher, C.; Hogan, T.; Polychroniadis, E. K.; Kanatzidis, M. G. *Science* **2004**, *303*, 818.

(8)   Hu, X.; Jood, P.; Ohta, M.; Kunii, M.; Nagase, K.; Nishiate, H.; Kanatzidis, M. G.; Yamamoto, A. *Energy Environ. Sci.* **2016**, *9*, 517.

(9)   Biswas, K.; He, J.; Blum, I. D.; Wu, C.-I.; Hogan, T. P.; Seidman, D. N.; Dravid, V. P.; Kanatzidis, M. G. *Nature* **2012**, *489*, 414.

(10) Biswas, K.; He, J.; Zhang, Q.; Wang, G.; Uher, C.; Dravid, V. P.; Kanatzidis, M. G. *Nat. Chem.* **2011**, *3*, 160.

(11) Gelbstein, Y.; Davidow, J.; Girard, S. N.; Chung, D. Y.; Kanatzidis, M. *Adv. Energy Mater.* **2013**, *3*, 815.

(12) Al Rahal Al Orabi, R.; Mecholsky, N. A.; Hwang, J.; Kim, W.; Rhyee, J. S.; Wee, D.; Fornari, M. *Chem. Mater.* **2016**, *28*, 376.

(13) Al Rahal Al Orabi, R.; Hwang, J.; Lin, C. C.; Gautier, R.; Fontaine, B.; Kim, W.;

Rhyee, J. S.; Wee, D.; Fornari, M. *Chem. Mater.* **2017**, *29*, 612.

(14) Liu, H.; Shi, X.; Xu, F.; Zhang, L.; Zhang, W.; Chen, L.; Li, Q.; Uher, C.; Day, T.; Snyder, G. J. *Nat Mater* **2012**, *11*, 422.

(15) Ge, Z.; Zhang, B.; Chen, Y.; Yu, Z.; Liu, Y.; Li, J.-F. *Chem. Commun.* **2011**, *47*, 12697.

(16) He, Y.; Day, T.; Zhang, T.; Liu, H.; Shi, X.; Chen, L.; Snyder, G. J. *Adv. Mater.* **2014**, *26*, 3974.

(17) Dennler, G.; Chmielowski, R.; Jacob, S.; Capet, F.; Roussel, P.; Zastrow, S.; Nielsch, K.; Opahle, I.; Madsen, G. K. H. *Adv. Energy Mater.* **2014**, *4*, 1301581.

(18) Suekuni, K.; Tsuruta, K.; Ariga, T.; Koyano, M. *Appl. Phys. Express* **2012**, *5*, 51201.

(19) Suekuni, K.; Tsuruta, K.; Kunii, M.; Nishiate, H.; Nishibori, E.; Maki, S.; Ohta, M.; Yamamoto, A.; Koyano, M. *J. Appl. Phys.* **2013**, *113* (4), 43712.

(20) Lu, X.; Morelli, D. T.; Xia, Y.; Zhou, F.; Ozolins, V.; Chi, H.; Zhou, X.; Uher, C. *Adv. Energy Mater.* **2013**, *3*, 342.

(21) Lara-Curzio, E.; May, A. F.; Delaire, O.; McGuire, M. A.; Lu, X.; Liu, C. Y.; Case, E. D.; Morelli, D. T. *J. Appl. Phys.* **2014**, *115*, 193515.

(22) Chetty, R.; Bali, A.; Naik, M. H.; Rogl, G.; Rogl, P.; Jain, M.; Suwas, S.; Mallik, R. C. *Acta Mater.* **2015**, *100*, 266.

(23) Bouyrie, Y.; Candolfi, C.; Ohorodniichuk, V.; Malaman, B.; Dauscher, A.; Tobola, J.; Lenoir, B. *J. Mater. Chem. C* **2015**, *3*, 10476.

(24) Bouyrie, Y.; Candolfi, C.; Dauscher, A.; Malaman, B.; Lenoir, B. *Chem. Mater.* **2015**,

27, 8354.

(25)   Barbier, T.; Lemoine, P.; Gascoin, S.; Lebedev, O. I.; Kaltzoglou, A.; Vaqueiro, P.; Powell, A. V.; Smith, R. I.; Guilmeau, E. *J. Alloys Compd.* **2015**, *634*, 253.

(26)   Barbier, T.; Rollin-Martinet, S.; Lemoine, P.; Gascoin, F.; Kaltzoglou, A.; Vaqueiro, P.; Powell, A. V.; Guilmeau, E. *J. Am. Ceram. Soc.* **2016**, *99*, 51.

(27)   Chetty, R.; Bali, A.; Mallik, R. C. *J. Mater. Chem. C* **2015**, *3*, 12364.

(28)   Kim, F. S.; Suekuni, K.; Nishiate, H.; Ohta, M.; Tanaka, H. I.; Takabatake, T. *J. Appl. Phys.* **2016**, *119*, 175105.

(29)   Suekuni, K.; Takabatake, T. *APL Mater.* **2016**, *4*, 104503.

(30)   Lu, X.; Morelli, D. T. *ed. C. Uher, (CRC Press. Taylor Fr. Group, Boca Raton, FL)* **2016**, *16*, 473.

(31)   Barbier, T.; Lemoine, P.; Martinet, S.; Eriksson, M.; Gilmas, M.; Hug, E.; Guélou, G.; Vaqueiro, P.; Powell, A. V; Guilmeau, E. *RSC Adv.* **2016**, *6*, 10044.

(32)   Suekuni, K.; Kim, F. S.; Nishiate, H.; Ohta, M.; Tanaka, H. I.; Takabatake, T. *Appl. Phys. Lett.* **2014**, *105*, 132107.

(33)   Suekuni, K.; Kim, F. S.; Takabatake, T. *J. Appl. Phys.* **2014**, *116*, 63706.

(34)   Pavan Kumar, V.; Paradis-Fortin, L.; Lemoine, P.; Caignaert, V.; Raveau, B.; Malaman, B.; Le Caër, G.; Cordier, S.; Guilmeau, E. *Inorg. Chem.* **2017**, *56*, 13376.

(35)   Qiu, P.; Zhang, T.; Qiu, Y.; Shi, X.; Chen, L. *Energy Environ. Sci.* **2014**, *7*, 4000.

(36)   Guélou, G.; Powell, A. V.; Vaqueiro, P. *J. Mater. Chem. C* **2015**, *3*, 10624.

(37)   Kumar, V. P.; Barbier, T.; Lemoine, P.; Raveau, B.; Nassif, V.; Guilmeau, E. *Dalt.*

Trans. **2017**, *46*, 2174.

(38) Pavan Kumar, V.; Barbier, T.; Raveau, B.; Daou, R.; Malaman, B.; Le Caër, G.; Lemoine, P.; Guilmeau, E. *J. Phys. Chem. C* **2017**.

(39) Shen, Y.; Li, C.; Huang, R.; Tian, R.; Ye, Y.; Pan, L.; Koumoto, K.; Zhang, R.; Wang, Y. *Sci. Rep.* **2016**, *6*, 32501.

(40) Liu, M. L.; Huang, F. Q.; Chen, L. D.; Chen, I. W. *Appl. Phys. Lett.* **2009**, *94*, 202103.

(41) Yang, H.; Jauregui, L. A.; Zhang, G.; Chen, Y. P.; Wu, Y. *Nano Lett.* **2012**, *12*, 540.

(42) Khan, A. U.; Al Rahal Al Orabi, R.; Pakdel, A.; Vaney, J.; Fontaine, B.; Gautier, R.; Halet, J.; Mitani, S.; Mori, T. *Chem. Mater.* **2017**, *29*, 2988.

(43) Bourgès, C.; Lemoine, P.; Lebedev, O. I.; Daou, R.; Hardy, V.; Malaman, B.; Guilmeau, E. *Acta Mater.* **2015**, *97*, 180.

(44) Tsujii, N.; Mori, T. *Appl. Phys. Express* **2013**, *6*, 43001.

(45) Xie, H.; Su, X.; Zheng, G.; Yan, Y.; Liu, W.; Tang, H.; Kanatzidis, M. G.; Uher, C.; Tang, X. *J. Phys. Chem. C* **2016**, *120*, 27895.

(46) Hashikuni, K.; Suekuni, K.; Usui, H.; Ohta, M.; Kuroki, K.; Takabatake, T. *Appl. Phys. Lett.* **2016**, *109*, 182110.

(47) Barbier, T.; Berthebaud, D.; Frésard, R.; Lebedev, O. I.; Guilmeau, E.; Eyert, V.; Maignan, A. *Inorg. Chem. Front.* **2017**, *4*, 424.

(48) Suekuni, K.; Tanaka, H. I.; Kim, F. S.; Umeo, K.; Takabatake, T. *J. Phys. Soc. Japan* **2015**, *84*, 103601.

(49) Lai, W.; Wang, Y.; Morelli, D. T.; Lu, X. *Adv. Funct. Mater.* **2015**, *25* (24), 3648.

(50) Kikuchi, Y.; Bouyrie, Y.; Ohta, M.; Suekuni, K.; Aihara, M.; Takabatake, T. *J. Mater. Chem. A* **2016**, *4* (39), 15207.

(51) Bourgès, C.; Gilmas, M.; Lemoine, P.; Mordvinova, N.; Lebedev, O. I.; Hug, E.; Nassif, V. M.; Malaman, B.; Daou, R.; Guilmeau, E. *J. Mater. Chem. C* **2016**, *4*, 7455.

(52) Spry, P. G.; Merlino, S.; Su Wang; Xiaomao Zhang; Buseck, P. R. *Am. Mineral.* **1994**, *79*, 750.

(53) Tan, G.; Hao, S.; Zhao, J.; Wolverton, C.; Kanatzidis, M. G. *J. Am. Chem. Soc.* **2017**, *139*, 6467.

(54) Lin, H.; Tan, G.; Shen, J. N.; Hao, S.; Wu, L. M.; Calta, N.; Malliakas, C.; Wang, S.; Uher, C.; Wolverton, C.; Kanatzidis, M. G. *Angew. Chemie - Int. Ed.* **2016**, *55*, 1.

(55) Vaqueiro, P.; Al Rahal Al Orabi, R.; Luu, S. D. N.; Guélou, G.; Powell, A. V.; Smith, R. I.; Song, J.-P.; Wee, D.; Fornari, M. *Phys. Chem. Chem. Phys.* **2015**, *17*, 31735.

(56) Christensen, M.; Abrahamsen, A. B.; Christensen, N. B.; Juranyi, F.; Andersen, N. H.; Lefmann, K.; Andreasson, J.; Bahl, C. R. H.; Iversen, B. B. *Nat. Mater.* **2008**, *7*, 811.

(57) Wee, D.; Kozinsky, B.; Fornari, M. *J. Phys. Soc. Japan* **2013**, *82*, 14602.

(58) Volja, D.; Kozinsky, B.; Li, A.; Wee, D.; Marzari, N.; Fornari, M. *Phys. Rev. B - Condens. Matter Mater. Phys.* **2012**, *85*, 245211.

(59) Al Rahal Al Orabi, R.; Orisakwe, E.; Wee, D.; Fontaine, B.; Gautier, R.; Halet, J.-F.; Fornari, M. *J. Mater. Chem. A* **2015**, *3*, 9945.

(60) Cahill, D. G.; Watson, S. K.; Pohl, R. O. *Phys. Rev. B* **1992**, *46*, 6131.

(61) Banik, A.; Vishal, B.; Perumal, S.; Datta, R.; Biswas, K. *Energy Environ. Sci.* **2016**, *9*,

2011.

(62)   Rodríguez-Carvajal, J. *Phys. B Condens. Matter* **1993**, *192* (1–2), 55.

(63)   Roisnel, T.; Rodríguez-Carvajal, J. *Mater. Sci. Forum* **2001**, *378–381*, 118.

(64)   Thompson, P.; Cox, D. E.; Hastings, J. B. *J. Appl. Crystallogr.* **1987**, *20* (2), 79.

(65)   Kim, H. S.; Gibbs, Z. M.; Tang, Y.; Wang, H.; Snyder, G. J. *APL Mater.* **2015**, *3*, 41506.

(66)   Alleno, E.; Bérardan, D.; Byl, C.; Candolfi, C.; Daou, R.; Decourt, R.; Guilmeau, E.; Hébert, S.; Hejtmanek, J.; Lenoir, B.; Masschelein, P.; Ohorodnichuk, V.; Pollet, M.; Populoh, S.; Ravot, D.; Rouleau, O.; Soulier, M. *Rev. Sci. Instrum.* **2015**, *86*, 11301.

(67)   Giannozzi, P.; Baroni, S.; Bonini, N.; Calandra, M.; Car, R.; Cavazzoni, C.; Ceresoli, D.; Chiarotti, G. L.; Cococcioni, M.; Dabo, I.; Corso, A. D.; Fabris, S.; Fratesi, G.; de Gironcoli, S.; Gebauer, R.; Gerstmann, U.; Gougoussis, C.; Kokalj, A.; Lazzeri, M.; Martin-Samos, L.; Marzari, N.; Mauri, F.; Mazzarello, R.; Paolini, S.; Pasquarello, A.; Paulatto, L.; Sbraccia, C.; Scandolo, S.; Sclauzero, G.; Seitsonen, A. P.; Smogunov, A.; Umari, P.; Wentzcovitch, R. M. **2009**, *21*, 395502.

(68)   Supka, A. R.; Lyons, T. E.; Liyanage, L.; D'Amico, P.; Al Rahal Al Orabi, R.; Mahatara, S.; Gopal, P.; Toher, C.; Ceresoli, D.; Calzolari, A.; Curtarolo, S.; Nardelli, M. B.; Fornari, M. *Comput. Mater. Sci.* **2017**, *136*, 76.

(69)   Agapito, L. A.; Ismail-Beigi, S.; Curtarolo, S.; Fornari, M.; Nardelli, M. B. *Phys. Rev. B* **2016**, *93*, 35104.

(70)   Agapito, L. A.; Curtarolo, S.; Nardelli, M. B. *Phys. Rev. X* **2015**, *5*, 11006.

(71)   D'Amico, P.; Agapito, L.; Catellani, A.; Ruini, A.; Curtarolo, S.; Fornari, M.; Nardelli,

M. B.; Calzolari, A. *Phys. Rev. B* **2016**, *94*, 165166.

Table of Content

Cédric Bourgès, Yohan Bouyrie, Andrew R. Supka, Rabih Al Rahal Al Orabi, Pierric Lemoine, Oleg I. Lebedev, Michihiro Ohta, Koichiro Suekuni, Vivian Nassif, Vincent Hardy, Ramzy Daou, Yuzuru Miyazaki, Marco Fornari and Emmanuel Guilmeau

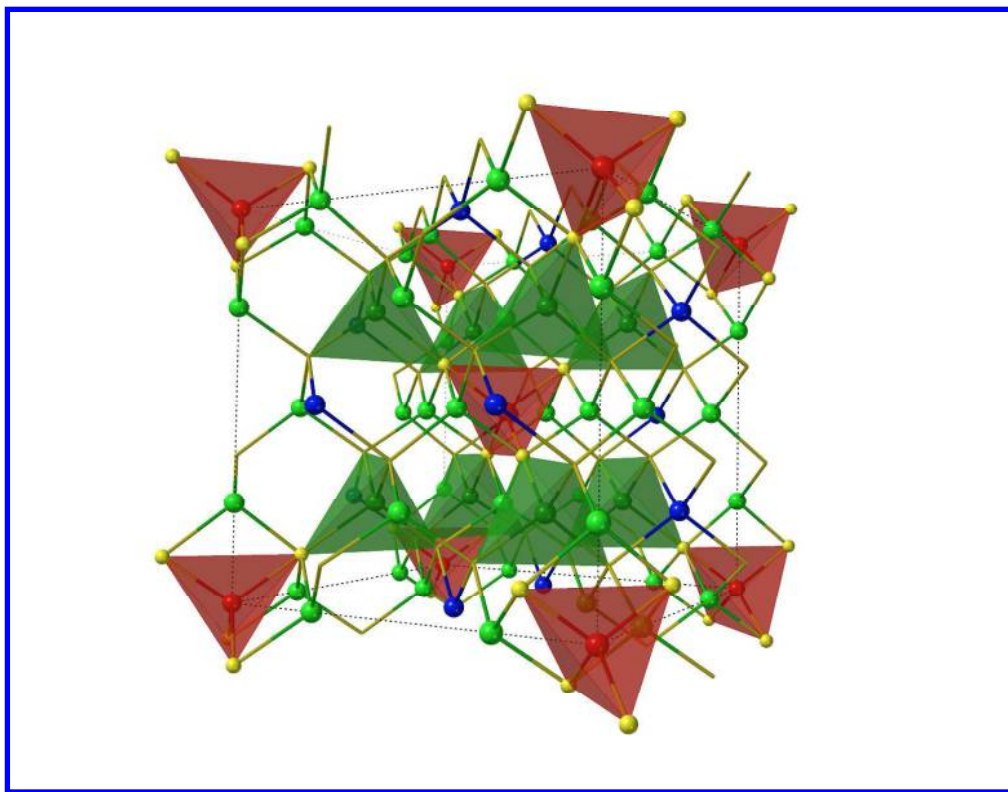**High-performance Thermoelectric Bulk Colusite by Process Controlled Structural Disordering**
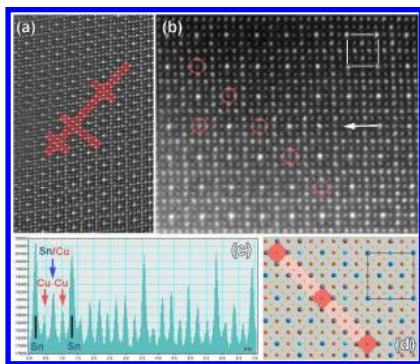
Figure 1. Unit cell of Cu26V2Sn6S32 (space group P4̄3n, N° 218). We show the S in 8e (yellow) bridging V (red) with Cu 8e (dark green). Cu in 6d and 12f are in light green, Sn in blue, and S in 24f are not shown. First principles computed structural parameters are in good agreement with experiments: a = 10.797 Å, Cu (12f, x = 0.748), Cu (8e, x = 0.753), Cu (6d), Sn (6c), V(2a), S (24i x = 0.867, y = 0.369, z = 0.119), and S (8e, x = 0.620).
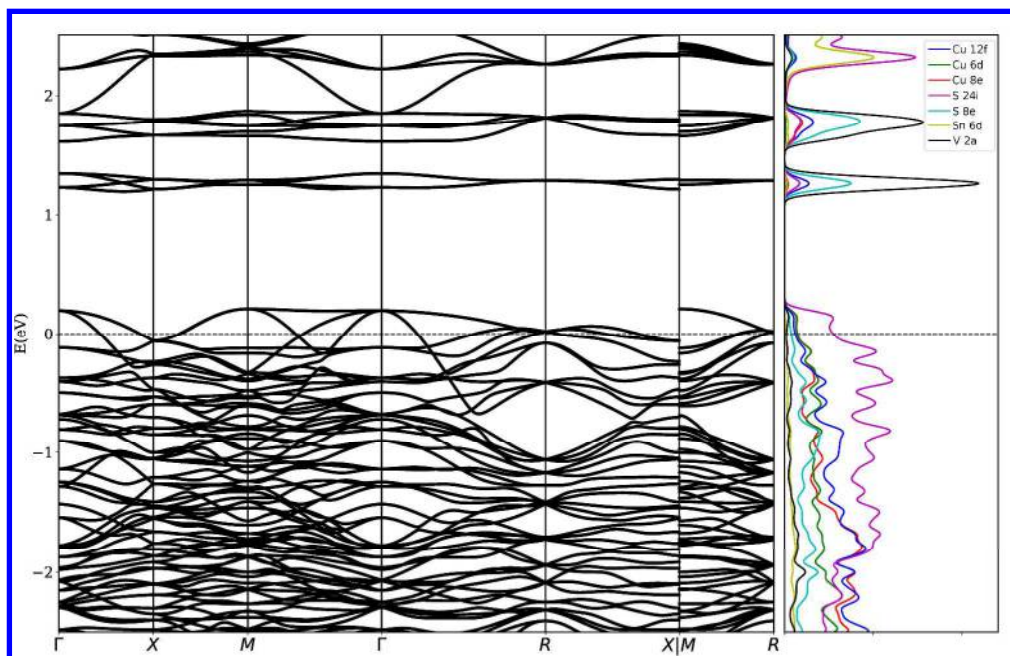
373x289mm (299 x 299 DPI)

Figure 2. Electronic band structure and atom projected electronic density of states of $Cu_{26}V_2Sn_6S_{32}$. Hubbard U corrections were computed self-consistently within the ACBN0 approach (see text): U(Cu in 12f) = 7.82, U(Cu in 8e) = 7.69, U(Cu in 6d) = 7.78, U(V) = 0.02, U(Sn) = 0.00, U(S in 24i) = 1.11 and U(S in 8e) = 1.13.
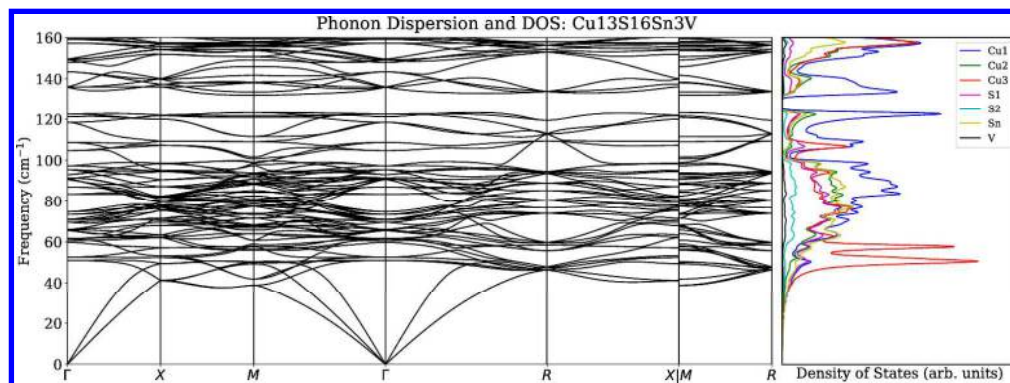
476x304mm (300 x 300 DPI)

Figure 3. Phonon dispersions and atom-projected vibrational density of states of Cu26V2Sn6S32. Optic modes at frequency as low as 40 cm-1 contribute to scattering phenomena that lower the lattice thermal conductivity. Notice the prominent role of Cu in 8e at low frequency.
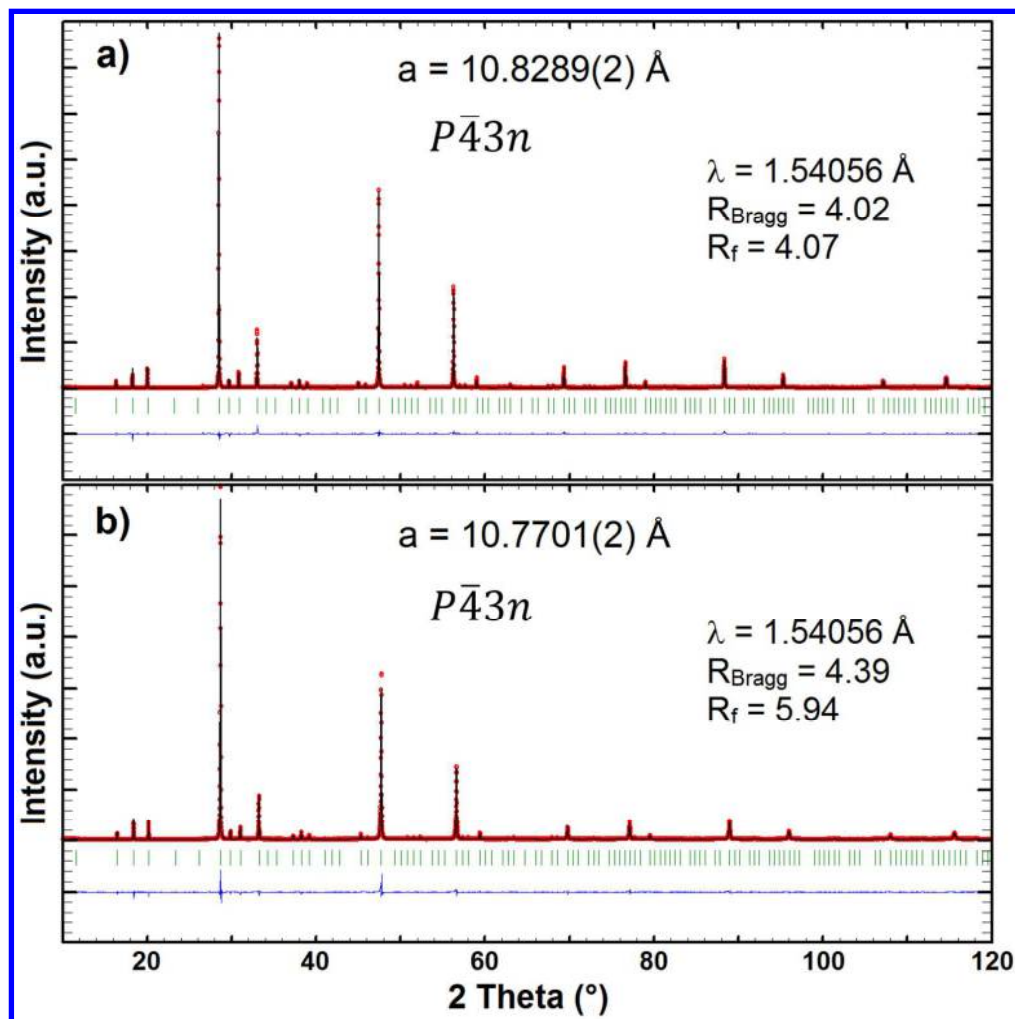
498x182mm (300 x 300 DPI)

Figure 4. Rietveld refinements of the XRPD patterns recorded at room temperature of the samples H (a) and L (b), sintered respectively at 1023 K and 873 K.
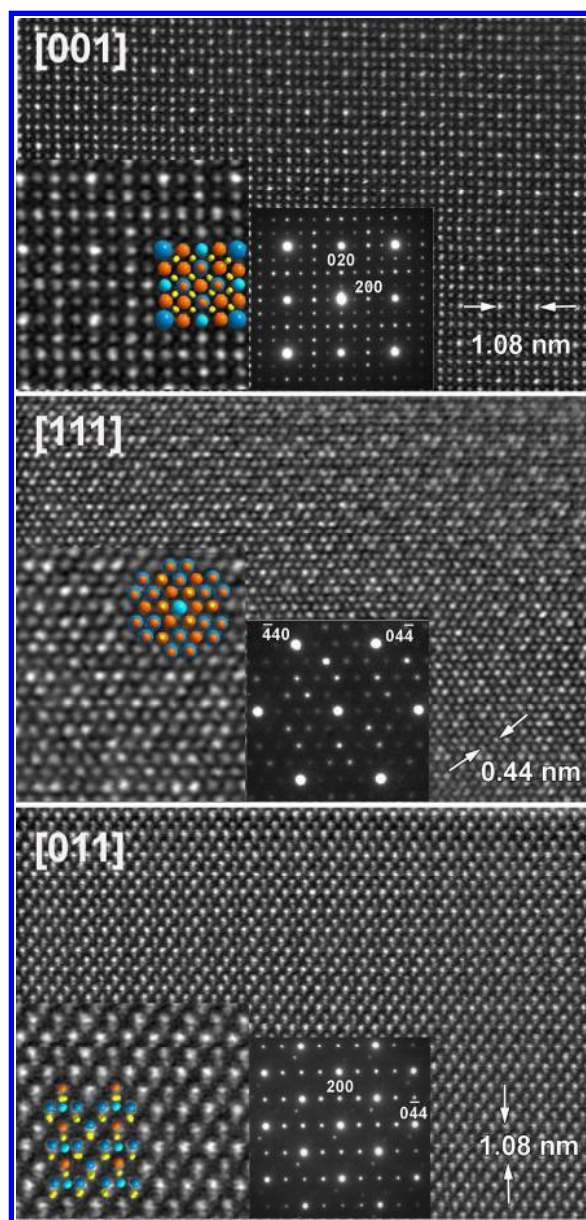
387x388mm (95 x 95 DPI)

Figure 5. Typical HAADF-STEM images and corresponding ED patterns of both samples L and H sintered respectively at 873 K or 1023 K for main zone axis [001], [111] and [011]. Enlargement images with the overlaid structural models are given as insert. (Sn-blue, V-light blue, Cu-orange, S-yellow)
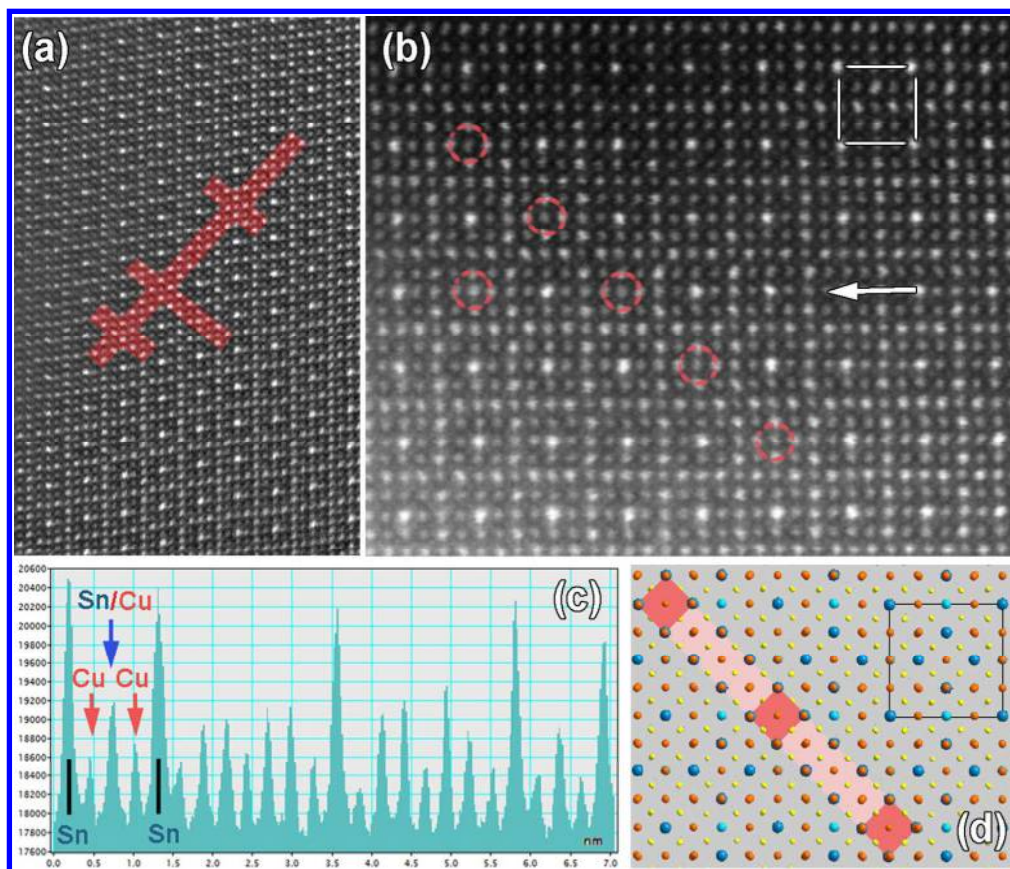
119x250mm (300 x 300 DPI)

Figure 6. (a) [001] HAADF-STEM image of sample H sintered at 1023 K. Red color indicates 1D line defects distributed within the perfect crystal of Cu26V2Sn6S32. (b) Enlargement part of line defect. Red circle depicted Sn-site defects columns. (c) Intensity line scan profile along the atomic layer indicated by white arrow in (b). There is a clear violation of Sn columns periodicity (higher peaks in the plot profile) corresponding to Sn-site defects. Note that the peak intensity of Sn-site defects columns is similar to those of pure Cu column suggesting the substitution of Sn by Cu atoms. (d) Corresponding structural model of the 1D Sn-vacancy line defect.
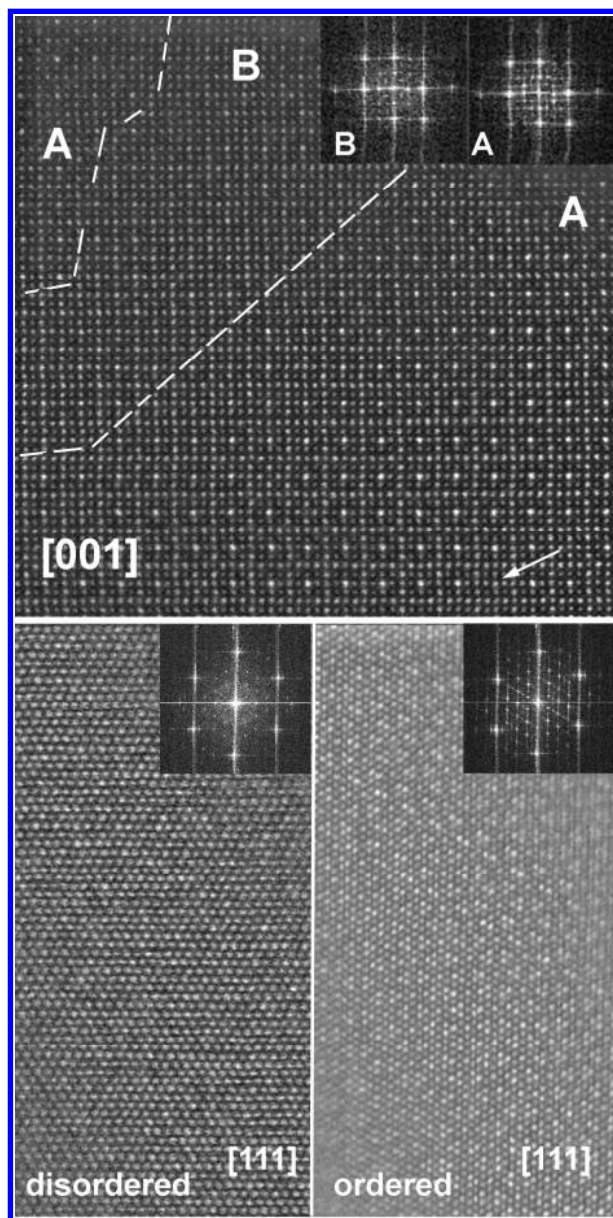
123x105mm (300 x 300 DPI)

Figure 7. [001] and [111] HAADF-STEM images showing the coexistence of ordered an disordered regions within the same crystallite in the sample H sintered at 1023 K. Corresponding FT patterns are given as inset. Row indicates a point defect.
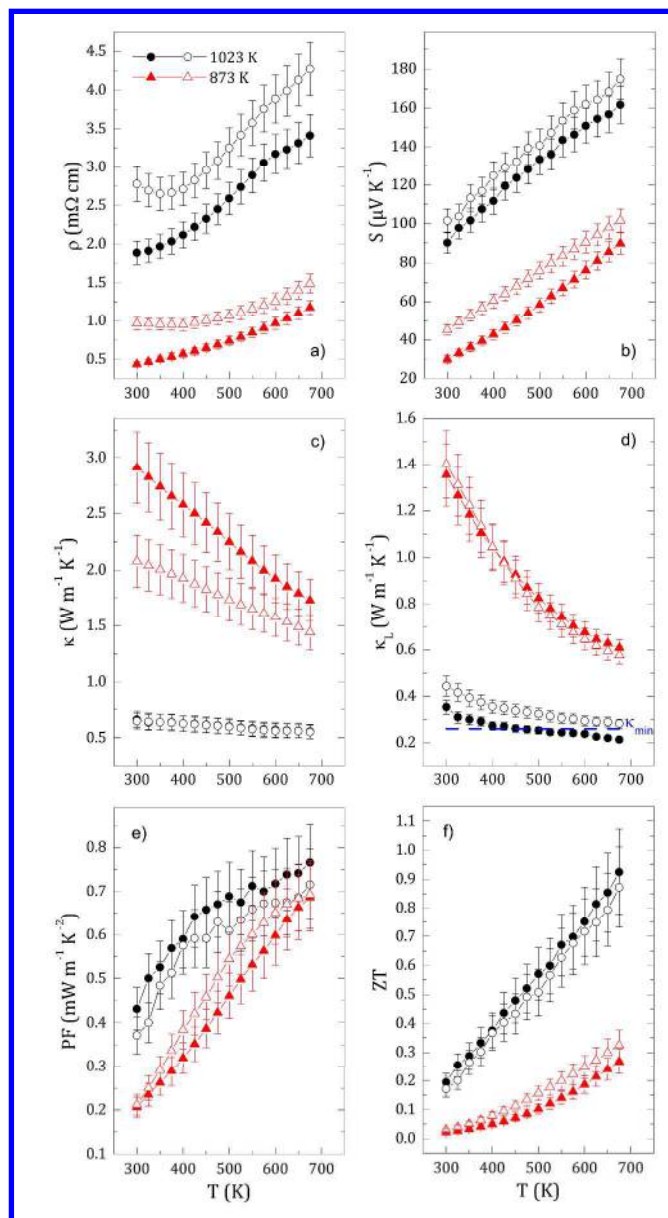
119x238mm (300 x 300 DPI)

Figure 8. Temperature dependence of a) electrical resistivity (ρ), b) Seebeck coefficient (S) c) thermal conductivity (κ), d) lattice thermal conductivity (κL), e) power factor (PF), and f) dimensionless figure of merit ZT of samples L and H, sintered at 873 K and 1023 K, respectively.

286x523mm (300 x 300 DPI)